J Mater Sci (2023) 58:1214–1228

Materials for life sciences

A pH-responsive CaO_2@ZIF-67 system endows a scaffold with chemodynamic therapy properties

Guowen Qian[1], Junzhe Wang[1], Liuyimei Yang[2], Zhikui Zeng[3], Zhenyu Zhao[4], Shuping Peng[5,6,*], and Cijun Shuai[1,7,*]

[1] *Institute of Additive Manufacturing, Jiangxi University of Science and Technology, Nanchang 330013, China*
[2] *Ganjiang Innovation Academy, Chinese Academy of Sciences, Ganzhou 341119, China*
[3] *Department of Orthopedics, The Affiliated Hospital of Jiangxi University of Chinese Medicine, Nanchang 330006, China*
[4] *Shenzhen Institute of Information Technology, School of Sino-German Robotics, Shenzhen 518172, China*
[5] *The Key Laboratory of Carcinogenesis and Cancer Invasion of the Chinese Ministry of Education, Xiangya Hospital, Central South University, Changsha 410078, Hunan, China*
[6] *NHC Key Laboratory of Carcinogenesis of Hunan Cancer Hospital and the Affiliated Cancer Hospital of Xiangya, School of Medicine, Cancer Research Institute, School of Basic Medical Science, Central South University, Changsha 410013, Hunan, China*
[7] *State Key Laboratory of High Performance Complex Manufacturing, Central South University, Changsha 410083, China*

Received: 8 September 2022
Accepted: 15 December 2022
Published online: 7 January 2023

ABSTRACT

The insufficient of H_2O_2 restricts the efficacy of chemodynamic therapy in tumor microenvironment. Calcium peroxide (CaO_2) is expected to solve this problem due to its H_2O_2-evolving ability. However, it prematurely decomposes in the moist air or water before reaching tumor site. In this study, zeolitic imidazolate framework-67 (ZIF-67) was in-situ grown on the surface of CaO_2 to construct a pH-responsive CaO_2@ZIF-67 system and then incorporated into poly-L-lactic acid (PLLA) to prepare PLLA/CaO_2@ZIF-67 scaffold by selective laser sintering technology. On the one hand, ZIF-67 is used as a chemodynamic therapy agent due to the release of cobalt ions after degradation. On the other hand, ZIF-67 can serve as protective layers to prevent premature decomposition of CaO_2 due to its hydrophobic properties, and then CaO_2 is exposed and reacts with water to form H_2O_2 after the pH-responsive degradation of ZIF-67 under tumor acidic microenvironment. Results showed that the PLLA/CaO_2@ZIF-67 scaffold could sustainedly produce H_2O_2 under acidic pH and achieve 84.64% antitumor ratio against MG-63 cells. In addition, the scaffold also promoted proliferation and osteogenic differentiation of mouse bone marrow mesenchymal stem cells due to the release of calcium ions. The prepared PLLA/CaO_2@ZIF-67 scaffold with chemodynamic antitumor and osteogenic effects has great potential to treat tumorous bone defect.

Handling Editor: Annela M. Seddon.

Address correspondence to E-mail: shuping@csu.edu.cn; shuai@csu.edu.cn

https://doi.org/10.1007/s10853-022-08103-w

Introduction

Chemodynamic therapy (CDT) based on Fenton/Fenton-like reactions, as a prospective alternative to traditional tumor therapies (e.g., surgery, radiotherapy, and chemotherapy), attracted great attention in recent years on account of the high selectivity and minimal side effects [1, 2]. Generally, CDT catalyzes hydrogen peroxide (H_2O_2) within tumor microenvironment through transition metal ions (e.g., Fe, Co, Ni, Cu, and Mn) to produce reactive oxygen species (ROS). ROS can destroy proteins, lipids and nucleic acids in tumor cells via oxidative stress, thus inducing tumor cell death [3–8]. However, the limited concentration of H_2O_2 in tumor microenvironment (50×10^{-6} to 100×10^{-6} M) limits the treatment efficacy of CDT [9–12]. Hence, it is of profound significance to explore ways to break the limit of H_2O_2 to enhance the efficacy of CDT.

The delivery of metal peroxide, such as calcium peroxide (CaO_2) [13], manganese peroxide (MnO_2) [14], copper peroxide (CuO_2) [15], etc., into tumors is an effective strategy to elevate the production of H_2O_2 [16]. Metal peroxide enables to release H_2O_2 under tumor acidic microenvironment based on the equation: $MO_2 + 2H^+ \rightarrow H_2O_2 + M^{2+}$ [17]. Among various metal peroxides, CaO_2, as H_2O_2-generating materials, has been widely reported because of its efficient H_2O_2-evolving ability and good biocompatibility [18]. He et al. [19] synthesized a solid lipid monostearin coated CaO_2 nanocarrier for the co-delivery of doxorubicin (DOX) and iron-oleate complex; the results showed that the nanocarrier could increase H_2O_2 levels and achieve highly efficient CDT. Liu et al. [20] reported a H_2O_2/O_2 self-supplying nanoagent with manganese silicate-supported CaO_2 and indocyanine green and found that CaO_2 within nanoagent reacts with water to produce O_2 and H_2O_2 for elevating ROS production. However, CaO_2 can decompose in the moist air or water, which compromises H_2O_2-generating effect before reaching the tumor site.

Based on the acidic tumor microenvironment [21–23], constructing a pH-responsive protective layer by in-situ growth is a prospect method to prevent the premature decomposition of CaO_2. Zeolitic imidazolate framework-67 (ZIF-67) is a typical metal–organic frameworks (MOFs) materials with periodic network structure formed by the self-assembly of 2-methylimidazole and cobalt (Co) ions, which recently attracts extensive attention of researchers as protective layer because of their hydrophobic properties and large surface area [24–26]. Moreover, ZIF-67 also possesses pH responsiveness due to the deprotonation of methylimidazole under acidic pH condition [27, 28]. More importantly, ZIF-67 is widely used as a CDT agent due to the release of Co ions after degradation, and Co ions can catalyze H_2O_2 to generate ·OH, thus achieving chemodynamic antitumor therapy [29]. In addition, ZIF-67 can in-situ grow on the surface of CaO_2 by ectopic nucleation and growth manner [15, 30].

In this study, ZIF-67 was in-situ grown on the surface of CaO_2 via solvothermal reaction to construct CaO_2@ZIF-67 system and then introduced into poly-L-lactic acid (PLLA) to prepare PLLA/CaO_2@-ZIF-67 scaffold by selective laser sintering technology [31–37]. Under acidic tumor microenvironment, ZIF-67 can decompose rapidly to release Co ions. And H_2O_2 is produced by the reaction between water and the exposed CaO_2, and then cobalt ions catalyze H_2O_2 to generate vast ROS, finally boosting H_2O_2-guided chemodynamic antitumor effect (Scheme 1). The morphology and microstructure of CaO_2@ZIF-67 were observed using transmission electron microscope (TEM). The pH-responsive release of Co ion and H_2O_2, reactive oxygen species (ROS) production, in vitro antitumor effect, and osteogenesis were researched systematically.

Materials and methods

Materials

Anhydrous calcium chloride ($CaCl_2$, AR), ammonia solution ($NH_3{\cdot}H_2O$, 25–28%), hydrogen peroxide aqueous solution (H_2O_2, 30%), polyethylene glycol (PEG 200), sodium hydroxide (NaOH, AR), methanol (AR), 2-methylimidazole ($C_4H_6N_2$, 98%), and cobalt nitrate hexahydrate ($Co(NO_3)_2{\cdot}6H_2O$, AR) were purchased from Shanghai Aladdin Biochemical Technology Co. Ltd. Titanic sulfate ($Ti(SO_4)_2$, ≥ 96%) was bought from Macklin Co. Ltd. Fetal bovine serum (FBS) was purchased from Cyagen Biosciences Inc., Dulbecco's modified of eagle's medium (DMEM) was bought from Beijing Solarbio Science & Technology Co., Ltd. The human osteosarcoma cell line MG-63 and mouse bone marrow mesenchymal stem cell line were purchased from ATCC (Manassas, VA, USA).

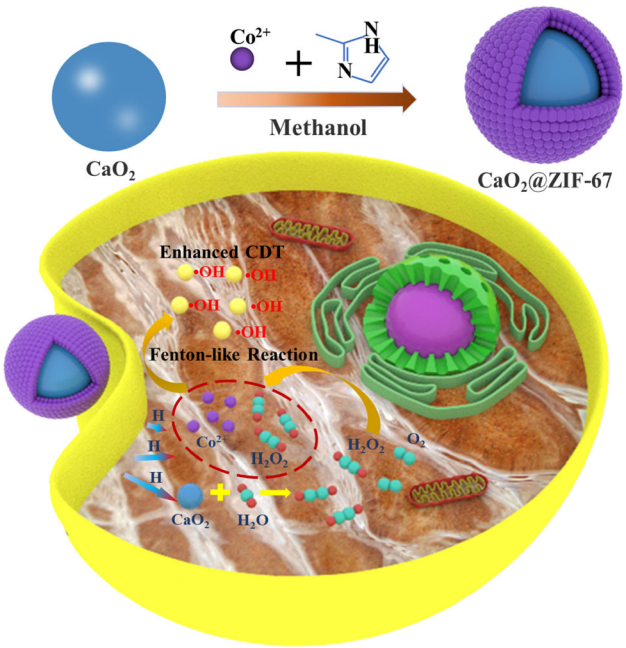

Scheme 1. Schematic diagram of synthesis and antitumor mechanism of CaO_2@ZIF-67.

Preparation of CaO_2 powders

3 g $CaCl_2$ was dissolved into 30 ml deionized water under constant agitation, then 15 ml (1 M) of ammonia water and 120 ml of PEG 200 were added into the above solution under stirred condition. Afterward, 15 ml of 30% H_2O_2 was added into the mixed solution at a rate of 3 drops per minute. The entire process was carried out at room temperature with continuous stirring and constant stirring velocity. After continuous stirring for 2 h, a faint yellow CaO_2 solution was obtained. Then NaOH solution (pH 13) was added into the CaO_2 solution until the pH of mixture came up to 11.5. The original mixture turned into white suspension after the addition of NaOH solution. Whereafter the mixture was centrifugated and collected the white precipitate and then washed with NaOH solution three times. Finally, distilled water was used to wash the precipitate until the final pH value was 8.4. The precipitate was collected and dried in a vacuum oven at 80 °C for 2 h so as to acquire CaO_2 powders.

Synthesis of ZIF-67 powders

ZIF-67 was synthesized by solvothermal reaction with Co^{2+} as the metal center and 2-methylimidazole as the organic ligand in methanol solution at room temperature. Specifically, 291 mg of $Co(NO_3)_2{\cdot}6H_2O$ and 660 mg of 2-methylimidazole were dissolved in 15 ml of methanol solution, respectively and then mixed the two solutions above and stirred for 15 min. The color of the mixture immediately turned purple, and then the mixture was left undisturbed for 6 h at room temperature. After centrifugation at 10,000 rpm for 5 min, the purple precipitate was collected, and then methanol was used to wash for three times and dried overnight at 80 °C in a vacuum drying oven to obtain ZIF-67 powders.

Construction of CaO_2@ZIF-67 powders

41 mg of CaO_2 was dispersed into 20 ml of methanol by ultrasonic treatment, and then 12 mg of $Co(NO_3)_2{\cdot}6H_2O$ was dissolved into the above solution, denoted as mixture A. 13 mg of 2-methylimidazole was dissolved in 20 ml of methanol, and clarified solution was obtained by ultrasonic treatment and denoted as mixture B. Afterward, mixture B was slowly added into mixture A and stirred for 2 h. The yellow-green precipitate was obtained by centrifugation and washed three times with methanol, and then CaO_2@ZIF-67 powders were obtained after vacuum drying at 50 °C for 4 h.

Preparation of scaffolds

Scaffolds were prepared by selective laser sintering (SLS) technology. Since the proportion of CaO_2 and ZIF-67 in the synthesized CaO_2@ZIF-67 was 80 wt% and 20 wt%, respectively, the specific composition of the powder of the four groups of scaffolds prepared was as follows: the four groups of powders were composed of 100 wt% PLLA, 96.8 wt% PLLA + 3.2 wt% CaO_2, 99.2 wt% PLLA + 0.8 wt% ZIF-67, and 96 wt% PLLA + 4 wt% CaO_2@ZIF-67. Firstly, the powders were mixed evenly by grinding. Secondly, SLS equipment was used to print the scaffold; specifically, the powders were evenly laid on the working platform and then selected a suitable porous scaffold model with three-dimensional interconnected pores and high porosity (60%). The porous structure of the scaffolds was conducive to the penetration of water into their inner part and transport of nutrients and the expulsion of metabolites; therefore, it was conducive to the adhesion and growth of cells. Afterward, SLS system was used to sinter the layer of powders, subsequently sintered layer by layer.

Finally, four different scaffolds were obtained successively.

Physicochemical characterization

Surface morphology of the powders was observed using scanning electron microscopy (SEM, EVO18, ZEISS, Germany). Transmission electron microscopy (TEM, FEI Talos F200S, USA) was used to observe the microstructure of the powders. X-ray diffraction (XRD, D8 Advance, Bruker Co., Germany) was used to analyze the phase of the samples. Fourier Transform Infrared Spectrometer (FTIR Spectrometer, FTIR-8050, Tian Jin Gang Dong Sci.&Tech, China) was applied to detect the functional groups of the prepared powders. X-ray photoelectron spectroscopy (XPS, Thermo Scientific K-Alpha, USA) was used to analyze the elemental composition and valence. Signal intensity of hydroxyl radical produced by the samples was verified by electron spin resonance (ESR, Bruker EMXnano, Bruker Co., Germany). Optical contact angle measuring instrument (DSA-Alpha, Betop Scientific, China) was utilized to measure the hydrophilicity of the scaffolds. The compression performances of the scaffolds were measured by a mechanical tester (CMTS5205, MTS, USA).

Ions release behavior

0.24 g of PLLA/CaO_2@ZIF-67 scaffolds was added into a 15 ml centrifuge tube, and then 8 ml of HCl-tris buffer was added. To evaluate the effect of different pH value on ion release, the 50 mM HCl-tris buffers with pH value of 5.0 and 6.5 were chosen. The soaking time was set as 0.5, 1, 3, 5, 7, and 14 days. The soaking liquid was collected and stored in a 4 °C refrigerator at predetermined time points, and then the fresh buffer was added into the tube and continue to the next soaking time point. Finally, inductively coupled plasma-optical emission spectroscopy (ICP-OES, Spectro Blue Sop, Germany) was applied to evaluate the calcium and cobalt ionic concentrations in the collected soaking liquids.

Hydrogen peroxide (H_2O_2) release

The production of H_2O_2 was measured using titanium sulfate microplate method. Titanium sulfate can react with H_2O_2 and generate yellow titanium peroxide complex (TiO_2^{2+}). The yellow depth of TiO_2^{2+} is linearly related to the concentration of hydrogen peroxide within limits, and the absorbance at 412 nm was measured by microplate reader (Varioskan LUX, Thermo Scientific, USA).

Cell behaviors

Cell culture

Human osteosarcoma MG-63 cells were selected as the typical in vitro model for bone tumor cell experiments. Mouse bone marrow mesenchymal stem cells (mBMSCs) were selected for osteogenesis experiment. The cells were cultured in High-Dulbecco's modified Eagle medium (H-DMEM) containing 10% fetal bovine serum at 37 °C in a cell incubator containing 5% carbon dioxide.

Antitumor experiments

Cell cytotoxicity and adhesion experiments. MG-63 cells were seeded in 48-well plates at a density of 10,000 cells per well. After one day of culture, four groups of scaffolds were added and cultured for one day. Then the toxicity of scaffolds to cells was determined. Cell counting kit (CCK-8) was used to detect cell activity, and the absorbance at 450 nm was measured by microplate reader. Cell status was observed by fluorescence microscope after live/dead cells staining; specifically, Calcein-AM and PI were used to confirm the visualized viability of cells. Then the fluorescence images were obtained by Olympus optical system (BX53F2, OLYMPUS, Japan).

Intracellular ROS production assay. MG-63 cells were seeded on 48-well plates at a density of 40,000 cells per well. After one day of culture, four group of scaffolds were added and then co-cultured for another day. 200 µl of the mixture of serum-free DMEM and DCFH-DA was added to each well (working concentration of DCFH-DA: 10 µmol/l) and then incubated for another 30 min, after which the intracellular ROS level was assessed by fluorescence microscopy (BX53F2, OLYMPUS, Japan).

Osteogenic experiments

Cell cytotoxicity and adhesion experiments. Firstly, the extracts were prepared as follows: 320 mg scaffolds of each group were soaked in 40 ml High-

Dulbecco's modified eagle medium (H-DMEM) containing 10% fetal bovine serum at 37 °C for one day, and then the extracts were collected and stored in a refrigerator at 4 °C for subsequent use. Secondly, mBMSCs were seeded in 96-well plates at a density of 3000 cells per well and cultured for 1 day. Then the medium was aspirated, and the extracts made of complete medium soaked by four groups of scaffolds were added and incubated for another one day and four days, respectively. After that, the effects of extracts on the cells were evaluated. CCK-8 assay was adopted to quantitatively analyze cell proliferation after treatment with the extracts, and the absorbance was measured by a microplate reader at 450 nm. Afterward, live/dead cell staining agent was used to stain the cells in a dark environment, and then morphology and number of cells were observed by a fluorescence microscope (BX53F2, OLYMPUS, Japan).

ALP staining test. Alkaline phosphatase (ALP) is an exoenzyme of osteoblasts, and its expression activity is an obvious feature of osteoblast differentiation. For purpose of verifying the effect of the extracts on the osteogenic differentiation of cells, alkaline phosphatase staining was performed. Firstly, mBMSCs were seeded on a 48-well plate at a density of 10,000 cells per well. The culture medium in the well plate was incubated with cells for one day and aspirated the medium in the well plate, then added the extracts prepared from the 4 sets of scaffolds in advance, and then incubated for an additional seven days. PBS was used to wash cells and then fixed with 4% paraformaldehyde for 30 min, subsequently removed the paraformaldehyde. After that, alkaline phosphatase was stained for 12 h in a 4 °C environment, and the staining results were observed with a microscope (BX53F2, OLYMPUS, Japan).

Alizarin Red S staining. In order to further investigate the effect of scaffolds on osteogenic differentiation of stem cells, Alizarin Red S staining was used to characterize the mineralization of osteogenic differentiation of stem cells. mBMSCs were firstly planted in 24-well plate at a density of 20,000 per well and then co-cultured with complete medium for one day. The complete medium was then aspirated and the extracts prepared from four different sets of scaffolds were added and cultured for another 14 days, during which fresh extracts needed to be replaced to ensure cells survival. After that, the extract was sucked out, the cells were washed with PBS twice and fixed with 4% paraformaldehyde for 30 min, then removed the paraformaldehyde and stained with Alizarin Red S dye for 30 min, washed gently with PBS three times, and finally, the staining results were observed with a microscope (BX53F2, OLYMPUS, Japan).

Statistic analysis

All data are expressed as means ± SD. At least three parallel samples were repeated for the quantitative experiments. The difference between two groups was analyzed by using Student's t-test. The results of $^{*}P < 0.05$ were considered to be statistically significant.

Results and discussion

Synthesis and characterization of powders

Calcium peroxide (CaO_2) was synthesized by hydrolyzation-precipitation method [38]. As shown in Fig. 1a, the synthesized CaO_2 particles displayed spherical morphology, and the average diameter of the particles was calculated as 2.5 μm. The transmission electron microscope (TEM) and corresponding selected area electron diffraction (SAED) images of the CaO_2 particles were exhibited in Figs. 1b, c. It could be seen that the surface of calcium peroxide particles was relatively rough, and the synthesized calcium peroxide was polycrystalline. After the in-situ growth of ZIF-67 on the surface of CaO_2, the size of CaO_2@ZIF-67 was larger than that of the CaO_2, and the average diameter of CaO_2@ZIF-67 particles was calculated as 3 μm (Fig. 1d). Moreover, a layer of substances with thickness of 250 nm was observed on the surface of CaO_2 (Fig. 1e). As can be seen from Fig. 1f, the synthesized CaO_2@ZIF-67 was also polycrystalline. In addition, the element mapping patterns further confirmed the existence of Ca, Co, C, N, and O elements and uniform dispersion on the surface of CaO_2 (Fig. 1g), demonstrating ZIF-67 was in-situ grown on the surface of CaO_2 successfully.

X-ray diffraction (XRD) was used to characterize the phase of the synthesized powders. The synthesized CaO_2 powder had characteristic peaks at 2θ value of 30°, 35°, 47°, 52°, and 60°, corresponding to (002), (110), (112), (103), and (202) crystal planes respectively, which were consistent with the standard structure of CaO_2 (JCPDS card No. 03–0865) (Fig. 2a).

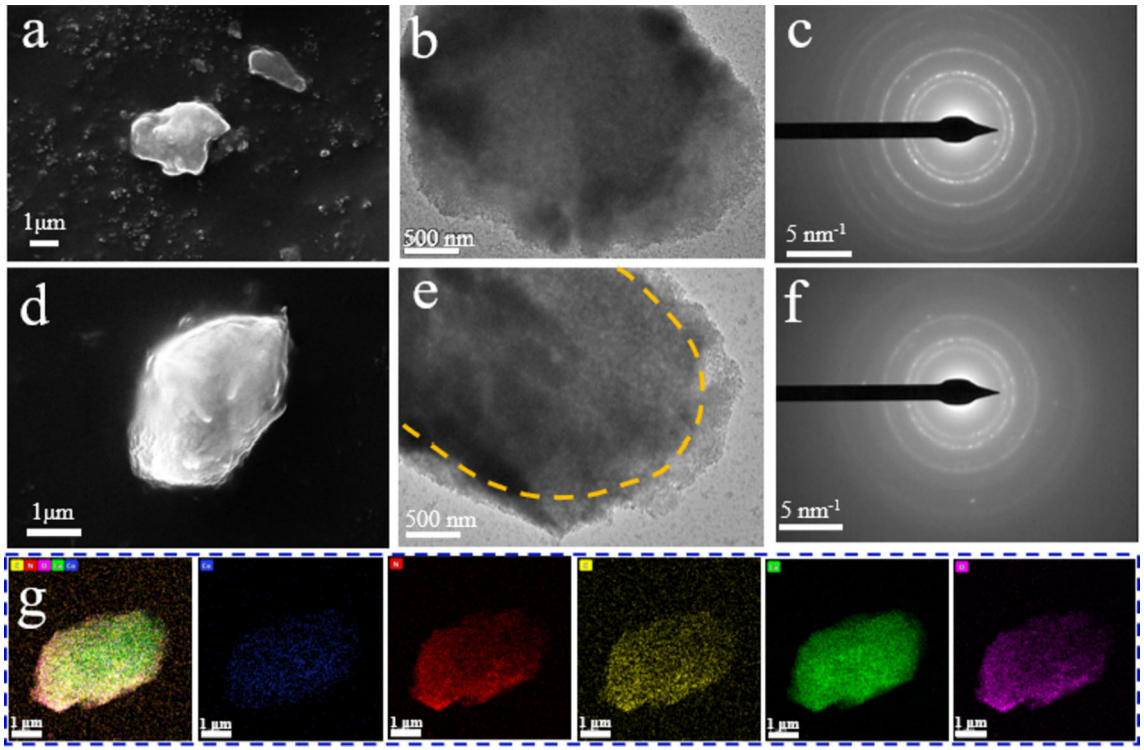

Figure 1 Characterization of CaO_2 and CaO_2@ZIF-67. **a** SEM, **b** TEM and corresponding **c** selected area electron diffraction images of CaO_2. **d** SEM, **e** TEM and corresponding **f** selected area electron diffraction images of CaO_2@ZIF-67. **g** Elemental mappings of CaO_2@ZIF-67.

The synthesized ZIF-67 had highly crystalline structure, and its diffraction peaks were corresponding well with XRD pattern of the standard simulation ZIF-67 (Fig. 2a). However, the characteristic peaks of the CaO_2@ZIF-67 powder were not obvious in the XRD pattern, which was due to that the ZIF-67 in-situ grown on the CaO_2 was the low crystallinity (Fig. 2a). In addition, the peaks of CaO_2 in the CaO_2@ZIF-67 XRD pattern were not visibly observed because of ZIF-67 grown on its surface.

Functional groups of the synthesized powders were analyzed by the Fourier transform infrared spectroscopy (FTIR) spectrum. As for FTIR spectrum of CaO_2, the peaks at 1420 and 875 cm^{-1} were consistent with the stretching vibration of O-Ca-O and O–O in CaO_2 [39, 40], respectively (Fig. 2b). In addition, the stretching vibration peak of C = N in 2-methylimidazole at 1385 cm^{-1} was observed in the FTIR spectrum of ZIF-67 [41] (Fig. 2b). By contrast, the stretching vibration peaks of O-Ca-O, O–O and C = N all appeared in the FTIR spectrum of CaO_2@-ZIF-67, showing ZIF-67 was in-situ grown on the surface of CaO_2 successfully (Fig. 2b).

X-ray photoelectron spectroscopy (XPS) analysis was carried out to further characterize the composition and valence state of the powders. The XPS spectrum showed that CaO_2@ZIF-67 contained C, Ca, N, O, Co elements (Fig. 2c). In Fig. 2d, there are two characteristic peaks at 345.68 eV (Ca 2p3/2) and 349.28 eV (Ca 2p1/2) in the high-resolution spectrum, indicating that this is Ca^{2+} [42]. The binding energy located at 532.28 eV was attributed to O_2^{2-} [43] (Fig. 2e). Two main photoelectron peaks at 779.78 eV and 795.28 eV in Fig. 2f were attributable to Co 2p3/2 and Co 2p1/2, respectively. Co (II) is the main form existing in CaO_2@ZIF-67 on account of the occurrence of the satellite peak (sat. 1, 784.98 eV) [44]. All the above analysis indicated that the CaO_2@ZIF-67 particles were synthesized successfully.

Performances of PLLA/CaO_2@ZIF-67 scaffolds

The PLLA/CaO_2@ZIF-67 scaffold was prepared using selective laser sintering (SLS) technology; then

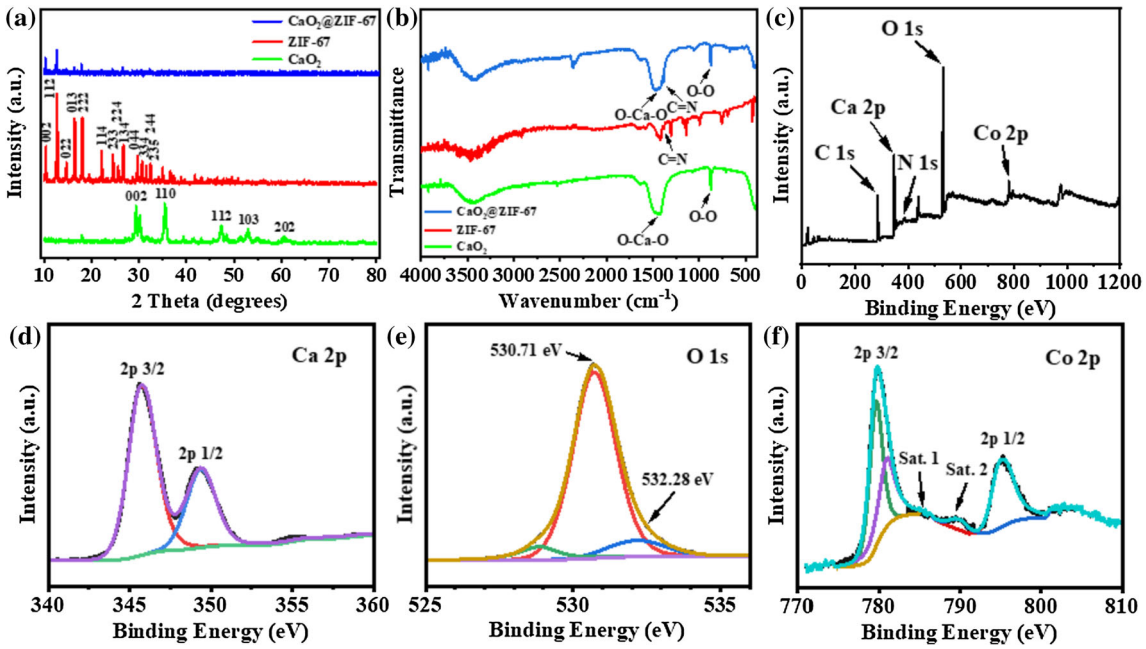

Figure 2 Characterization of CaO_2 and CaO_2@ZIF-67. **a** XRD spectra of CaO_2, ZIF-67 and CaO_2@ZIF-67. **b** FTIR spectra of CaO_2, ZIF-67 and CaO_2@ZIF-67. **c** XPS spectrum of CaO_2@ZIF-67. **d** XPS high-resolution spectrum of Ca 2p; **e** O 1 s; **f** Co 2p.

ionic release, H_2O_2 and ·OH productions of the scaffold after immersion in buffers were evaluated. Considering acidic tumor microenvironment and pH-responsive effect of ZIF-67, the buffers with different pH value (5.0 and 6.5) were chosen as the immersion solution. The release of Co^{2+} and Ca^{2+} from CaO_2@ZIF-67 after immersion in the buffers with different pH value was measured using inductively coupled plasma-optical emission spectroscopy (ICP-OES). As shown in Fig. 3a, b, the release profiles of Co^{2+} and Ca^{2+} mainly divided into two phases, including rapid and slow-release phases. A rapid release metal ions during the first 0 to 3 days appeared, and then the release rate gradually slowed down after immersion for three days. The release rate of Co^{2+} and Ca^{2+} at pH 5.0 was significantly faster than that at pH 6.5, and the release amount at pH 5.0 was also higher than that at pH 6.5. When the immersion time was 14 days at pH 5.0, the concentration of Co^{2+} and Ca^{2+} released from PLLA/CaO_2@ZIF-67 was 33.7 μg/ml and 342.4 μg/ml, respectively. By contrast, after immersion in the buffer at pH 6.5 for 14 days, the concentration of Co^{2+} and Ca^{2+} released from PLLA/CaO_2@ZIF-67 was 21.76 μg/ml and 92.5 μg/ml, respectively. These results suggested that ion release was related to pH value because of the pH responsiveness of ZIF-67. It is well known that ZIF-67 is stable under neutral condition, while it can decompose rapidly and release Co^{2+} under acidic condition due to the deprotonation of 2-methylimidazole under acid condition [27, 28]. Therefore, ZIF-67 can serve as protective layer to prevent premature breakdown of CaO_2 before the implantation of PLLA/CaO_2@ZIF-67 scaffold.

The fast decomposition of ZIF-67 under acidic tumor microenvironment generates Co^{2+}, which can then catalyze H_2O_2 and produce ·OH via a Fenton-like reaction, thus realizing chemodynamic antitumor. However, the insufficient H_2O_2 concentration in tumor cells (50×10^{-6}—100×10^{-6} M) declines the efficiency of chemodynamic antitumor. Therefore, CaO_2, acted as a H_2O_2 generator, was incorporated into bone scaffold. The main mechanism of producing H_2O_2 from CaO_2 is that CaO_2 can dissolve into water to form H_2O_2 under an acidic tumor environment based on the equation: $CaO_2 + 2H_2O \rightarrow H_2O_2 + Ca(OH)_2$. CaO_2@ZIF-67 was designed through in-situ grown ZIF-67 on CaO_2 and can synergistically boost chemodynamic antitumor effect. On the one hand, CaO_2 enables to provide H_2O_2 for chemodynamic therapy. On the other hand, ZIF-67 can serve as protective layer to prevent premature decomposition of CaO_2. Subsequently, the ability to produce H_2O_2 of the PLLA/CaO_2@ZIF-67 scaffold in different pH solutions was evaluated. The amount of H_2O_2

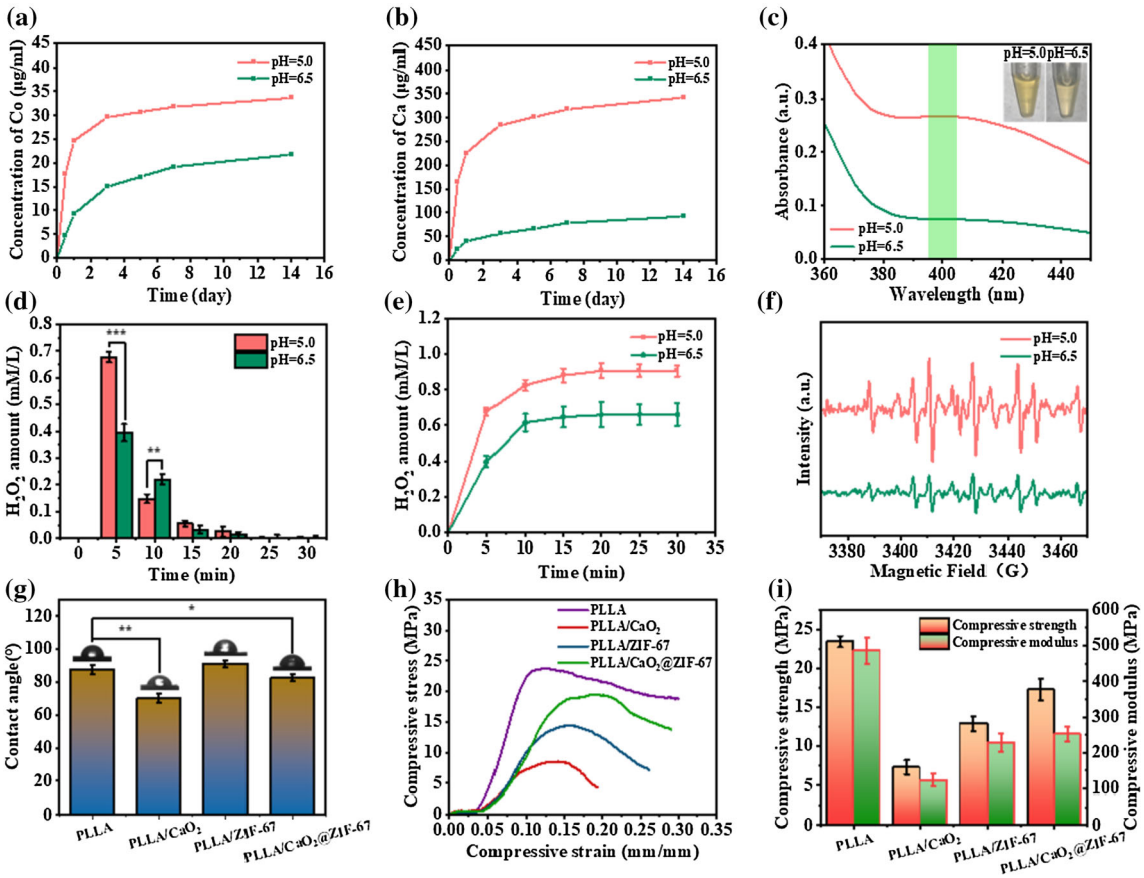

Figure 3 Performances of PLLA/CaO_2@ZIF-67 scaffolds. **a** Co^{2+} and **b** Ca^{2+} concentrations released from the PLLA/CaO_2@ZIF-67 scaffolds after immersion in buffers with different pH values for different time. **c** Absorbance spectrum of the titanium peroxide complex in the presence of PLLA/CaO_2@ZIF-67 scaffolds. **d** Stepwise and **e** cumulative release amount of H_2O_2 by PLLA/CaO_2@ZIF-67 scaffolds in buffers with different pH values. **f** ESR spectra of ·OH induced by PLLA/CaO_2@ZIF-67 in buffers with different pH values. **g** Water contact angels of scaffolds. **h** Compressive stress–strain curves and **i** compressive strengths and compressive moduli of four group of scaffolds. *p* values were calculated by Student's *t*-test ($^*p < 0.05$; $^{**}p < 0.01$; $^{***}p < 0.001$).

was detected using titanium sulfate microplate method. Because titanic sulfate can react with H_2O_2, to form yellow titanium peroxide complex (TiO_2^{2+}). The color depth of TiO_2^{2+} solution is linearly related with its optical density value at 412 nm, thus enabling to calculate the concentration of H_2O_2 (Fig. 3c). As shown in Fig. 3d, e, H_2O_2 amount in the buffers first increased rapidly during the immersion period of 0–10 min and then increased slowly and finally tended to be stable. At any times of immersion except for 10 min, the H_2O_2 yield at pH 5.0 was higher than that at pH 6.5. However, when the immersion was 10 min, the H_2O_2 amount at pH 6.5 was higher than that at pH 5.0. The probable reason was that when the PLLA/CaO_2@ZIF-67 scaffold was immersed in the buffer at pH 5.0, most ZIF-67 grown on the CaO_2 was degraded in the early stage and then exposed CaO_2 quickly reacted with water to generate vast H_2O_2. By contrast, when the pH value of the buffer was 6.5, a relatively small amount of ZIF-67 was degraded after immersion for 5 min. And most CaO_2 was still protected by ZIF-67; thus, the yield of H_2O_2 was lower than that at pH 5.0. However, with the prolongation of immersion time, ZIF-67 grown on CaO_2 gradually degraded, and more remaining CaO_2 at pH 6.5 was exposed than that at pH 5.0, thus generating more H_2O_2 at the immersion time of 10 min. It was worth noting that the cumulative release amount of H_2O_2 for the pH 5.0 buffer was greater than that for the pH 6.5 buffer at any immersion time.

The critical weapon of killing tumor is reactive oxygen species (ROS); therefore, the ·OH generated by a Fenton-like reaction of Co^{2+} and H_2O_2 was

detected using electron spin resonance (ESR) spectroscopy. Meanwhile, 5,5-dimethyl-1-pyrroline N-oxide (DMPO) was selected as a ·OH free radical trapping agent. As shown in Fig. 3f, the stronger intensity of 1:2:2:1 four-line characteristic signals for the buffer at pH 5.0 was detected compared with that at pH 6.5, suggesting generating more ·OH.

Next, the hydrophilic properties of the scaffolds were investigated. As shown in Fig. 3g, the hydrophobicity of the PLLA/ZIF-67 group was the highest, followed by the PLLA group, and the PLLA/CaO_2 group owned the best hydrophilicity with a water contact angle of about 70°. The water contact angle of the PLLA/CaO_2@ZIF-67 scaffold was 82.46°, which decreased compared to PLLA scaffold, indicating the addition of CaO_2@ZIF-67 improved the hydrophilicity of PLLA scaffold. By contrast, the hydrophilicity of the PLLA/CaO_2@ZIF-67 scaffold decreased compared to the PLLA/CaO_2 scaffold, which was due to the growth of hydrophobic ZIF-67 on the surface of the hydrophilic CaO_2, and ZIF-67 played a role in preventing the premature decomposition of CaO_2. The increased hydrophilicity also facilitated the full reaction of CaO_2 with water to produce hydrogen peroxide to improve the antitumor efficacy of chemodynamic therapy, meanwhile the hydrophilic scaffold surface facilitated the adhesion and proliferation of cells [45].

Finally, we also studied the mechanical properties of the scaffolds. Adequate mechanical properties are essential for bone repair. Scaffolds need sufficient mechanical strength to support the body, and appropriate porosity is conducive to cell adhesion and proliferation, new bone growth, and the formation of blood vessels [46]. The stress–strain curves of the scaffolds are displayed in Fig. 3h. The compressive stress of all scaffolds increased rapidly with increasing of compressive strain in the initial stage and then decreased slowly after reaching the yield strength. The compressive strength and compression modulus of scaffolds are shown in Fig. 3i. It can be seen that the pure PLLA scaffold possessed the highest compressive strength and modulus, while the PLLA/CaO_2 scaffold had the lowest compressive strength and modulus. The compressive strength and modulus of the PLLA/ZIF-67 scaffold were higher than that of the PLLA/CaO_2 scaffold. The mechanical properties of PLLA/CaO_2@ZIF-67 were better than that of the PLLA/CaO_2 and PLLA/ZIF-67 scaffolds, which were probably attributed to that CaO_2 tended to aggregate and disperse unevenly in the PLLA matrix. ZIF-67 has many organic ligands, which possesses good compatible with PLLA matrix. Meanwhile, the amino group of ZIF-67 could form a strong hydrogen bond with carboxyl group of PLLA [8, 47]. Therefore, the good interfacial bonding between CaO_2@ZIF-67 and PLLA matrix could be formed when the growth of ZIF-67 on the surface of CaO_2, which was attributed to improve the mechanical properties of the composite scaffold through a dispersion strengthening manner.

In vitro antitumor experiments

On account of effective hydroxyl radical generation, the in vitro antitumor effect was evaluated. Live/dead fluorescence staining images of MG-63 cells co-cultured with different scaffolds for one day are shown in Fig. 4a. Lots of green fluorescent dots were observed for the PLLA and PLLA/CaO_2 scaffolds, indicating that there were almost no apoptotic cells grown on these scaffolds. By contrast, in the case of PLLA/ZIF-67 and PLLA/CaO_2@ZIF-67 scaffolds, there were many red fluorescent dots, showing that most cells grown on these scaffolds were dead. Moreover, the number of dead cells grown on the PLLA/CaO_2@ZIF-67 scaffold was most.

In addition, the tumor cell killing rate of the scaffolds was calculated. First, the cytotoxicity of MG-63 cells co-cultured with four scaffolds for one day was evaluated by Cell Counting Kit-8 (CCK-8) assay, and the absorbance values were obtained. The lower the absorbance value, the higher the amount of apoptosis. The relative cell killing rate was then calculated using the following formula: relative cell killing rate = ($(CCK8_{PLLA}\text{-}CCK8_{Blank})$—$(CCK8_{experimental}\text{-}CCK8_{Blank})$) / $(CCK8_{PLLA}\text{-}CCK8_{Blank}) \times 100\%$, where $CCK8_{PLLA}$, $CCK8_{Blank}$, and $CCK8_{experimental}$ refer to the absorbance of PLLA scaffold co-cultured with MG-63 cells, blank group with complete medium and different scaffolds co-cultured with MG-63 cells, respectively.

The results are shown in Fig. 4b. Compared with PLLA group, the antitumor effect of PLLA/CaO_2 group was not obvious, while PLLA/ZIF-67 group had a relative tumor killing rate of 38.76% and thus owned a relatively obvious antitumor effect, whereas the PLLA/CaO_2@ZIF-67 group possessed the best antitumor effect with relative tumor killing rate of 84.64%. This is owing to the degradation of

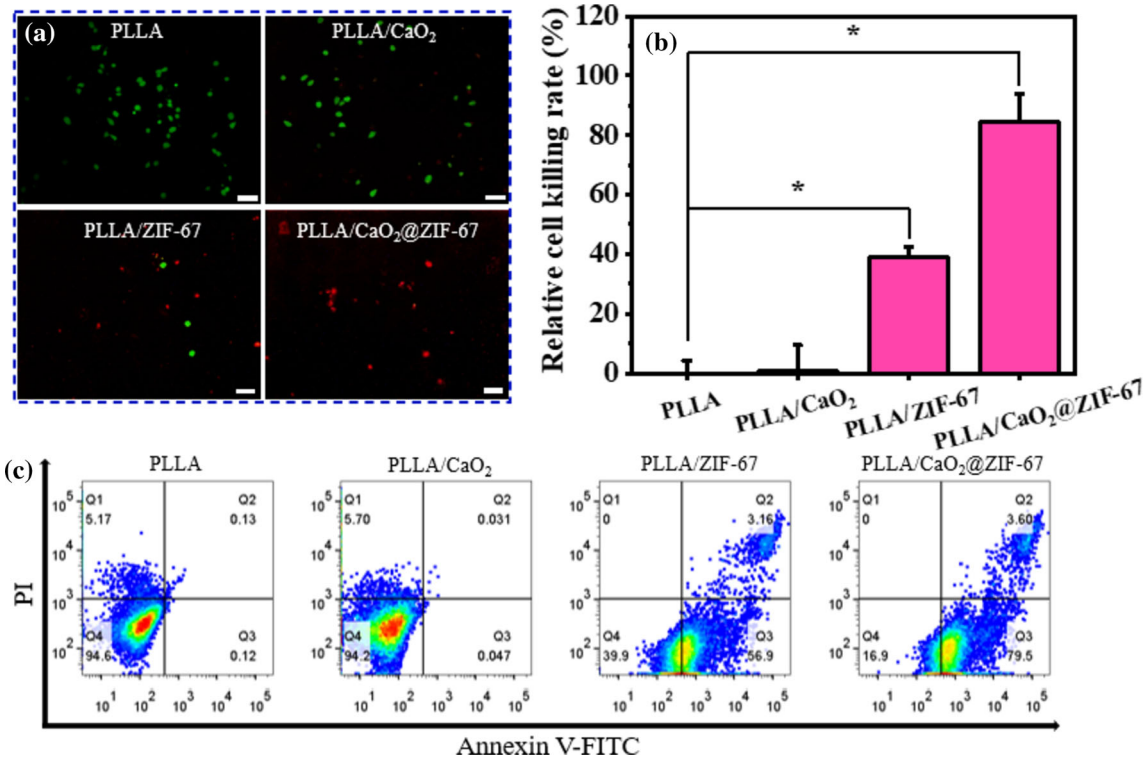

Figure 4 Antitumor properties of scaffolds. **a** Live/dead fluorescence staining images of MG-63 cells co-cultured with different scaffolds for 1 day. Scale bars are 100 μm. **b** Relative cell killing rates of MG-63 cells co-cultured with different scaffolds for 1 day. **c** Flow cytometry results of MG-63 cells cultured with different scaffolds for 1 day. p values were calculated by Student's t-test ($^{*}p < 0.05$; $^{**}p < 0.01$; $^{***}p < 0.001$).

CaO_2@ZIF-67 in the composite scaffold could produce cobalt ions and H_2O_2, and then cobalt ions converted H_2O_2 to ·OH through Fenton-like reaction, thus killing tumor cells.

Flow cytometry was used to detect cell apoptotic cycle. Annexin V and propidium iodide (PI) staining assay was used to identify the apoptosis of MG-63 cells grown on the scaffolds. As shown in Fig. 4c, many cells for the PLLA/ZIF-67 and PLLA/CaO_2@-ZIF-67 scaffolds displayed apoptotic state on day 1, while almost no apoptotic cells were visible for the PLLA and PLLA/CaO_2 scaffolds. The PLLA/CaO_2@ZIF-67 scaffold had the highest percentage of apoptotic cells. And the apoptotic cell percentage for the PLLA, PLLA/CaO_2, PLLA/ZIF-67, and PLLA/CaO_2@ZIF-67 groups was 0.12, 0.047, 56.9, and 79.5%, respectively.

The intracellular production of hydroxyl radicals(·OH) was verified by utilize ROS fluorescent probe 2′,7′-Dichlorofluorescin diacetate (DCFH-DA). DCFH-DA cross the cell membrane freely and is hydrolyzed by esterase in the cell to form DCFH, which cannot penetrate the cell membrane and thus remains in cells. Although DCFH-DA itself does not have fluorescence, non-fluoresce DCFH can be oxidized by intracellular ROS to produce DCF, which is fluorescent. Therefore, detecting the fluorescence of DCF, we can estimate the level of intracellular ROS. As shown in Fig. 5a, the PLLA group had weak fluorescence, while the PLLA/CaO_2 and PLLA/ZIF-67 groups possessed relatively strong green fluorescence. By contrast, the strongest fluorescent signal was detected for the PLLA/CaO_2@ZIF-67 group (Fig. 5b). CaO_2 can produce H_2O_2 under tumor acidic microenvironment, and H_2O_2 itself also gradually converts to ·OH in some degree. Therefore, some green fluorescent dots were visible for the PLLA/CaO_2 group. The generation of ·OH for the PLLA/ZIF-67 group was attributed to Fenton-like reaction between cobalt ions and endogenous H_2O_2 within cells. However, the amount of endogenous H_2O_2 was limited; thereby, the yield of ·OH was not enough to kill tumor cells effectively. By contrast, the PLLA/CaO_2@ZIF-67 group itself could produce cobalt ions

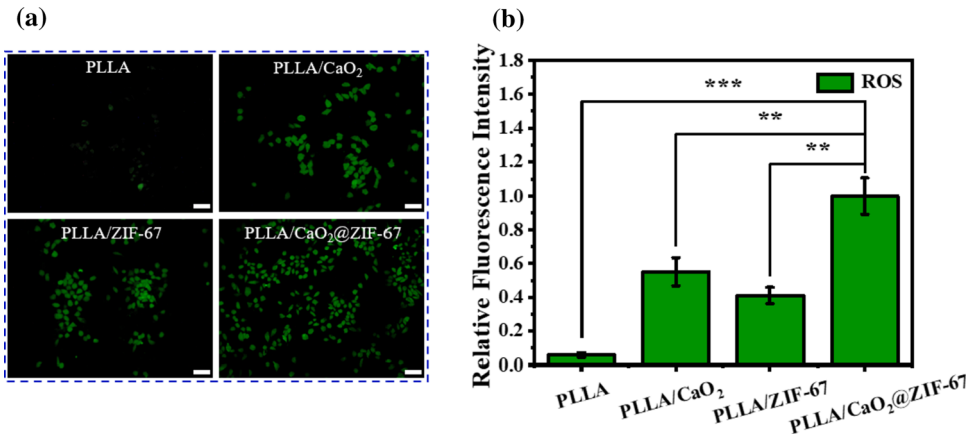

Figure 5 Antitumor mechanisms of ·OH production. **a** ROS fluorescence of MG-63 cells cultured with the PLLA, PLLA/CaO_2, PLLA/ZIF-67 and PLLA/CaO_2@ZIF-67 scaffolds, scale bars are 100 μm. **b** Statistical results of the fluorescence intensity of MG-63 cells cultured with different scaffolds treated with different scaffolds using Image J software. p values were calculated by Student's t-test (*$p < 0.05$; **$p < 0.01$; ***$p < 0.001$).

and H_2O_2, which were needed for the chemodynamic reaction. Therefore, the strongest green fluorescence was measured for the PLLA/CaO_2@ZIF-67 group. Considering the inhibitory effect of cobalt ion [48] and ·OH on tumor cells, the antitumor effect of PLLA/ZIF-67 group is slightly stronger than PLLA/CaO_2 group in spite of its relatively strong fluorescent intensity (Fig. 5b).

Osteogenic experiments

Mouse bone marrow mesenchymal stem cells (mBMSCs) are selected to evaluate the cytocompatibility and osteogenic effects of the scaffolds [49]. The living/dead fluorescent staining images of mBMSCs cultured with different scaffolds for four days are shown in Fig. 6a. Most green and little red fluorescent dots were observed for all groups, indicating that all scaffolds had no cytotoxicity and possessed good biological safety. To quantitatively measure the proliferative capacity of the cells grown on the scaffolds, a CCK-8 assay was performed. As shown in Fig. 6b, the values of CCK-8 assay of four groups after one day of incubation were relatively close and low, and the values in PLLA/CaO_2 and PLLA/CaO_2@ZIF-67 groups were slightly higher than those in the other two groups. On the four days of co-cultivation, the cell number for all groups increased evidently, demonstrating that all scaffolds had good cytocompatibility. And the cell number for the PLLA/CaO_2 and PLLA/CaO_2@ZIF-67 group was more numerous than that for the other two groups. In addition, the PLLA/CaO_2 group had the best promoting cell proliferation effect, which was due to the promoting effect of the released calcium ions on cell proliferation.

One of the prominent markers of early osteogenic differentiation is the expression of alkaline phosphatase (ALP) [50]. The expression of ALP reflects the differentiation level of osteoblasts. Hence, ALP staining experiment was carried out for purpose of studying the effect of scaffolds on osteogenic differentiation. As shown in Fig. 6c, PLLA/CaO_2 group displayed the most purple areas, representing the highest expression of ALP, followed by PLLA/CaO_2@ZIF-67 group. The probable reason was the ability of calcium ions released from these scaffolds to regulate cell proliferation and osteogenic differentiation [51, 52]. Figure 6d exhibits the statistical analysis of ALP expression of mBMSCs cultured with different scaffolds, which was consistent with the ALP staining results.

Calcium deposition is also one of the prominent marker events of osteogenic differentiation of stem cells [53]. Stem cells can differentiate into osteoblasts and form calcium nodules. Since Alizarin Red S dye chelates with calcium to form red complex, Alizarin Red S staining is often applied to indirectly reflecting the level of cell differentiation. As can be seen from Fig. 6e, PLLA/CaO_2 group owned the largest area of red region, followed by PLLA/CaO_2@ZIF-67 group, and the area of red region in PLLA/ZIF-67 group was less than that in PLLA group. This is owning to calcium ions released from scaffolds significantly

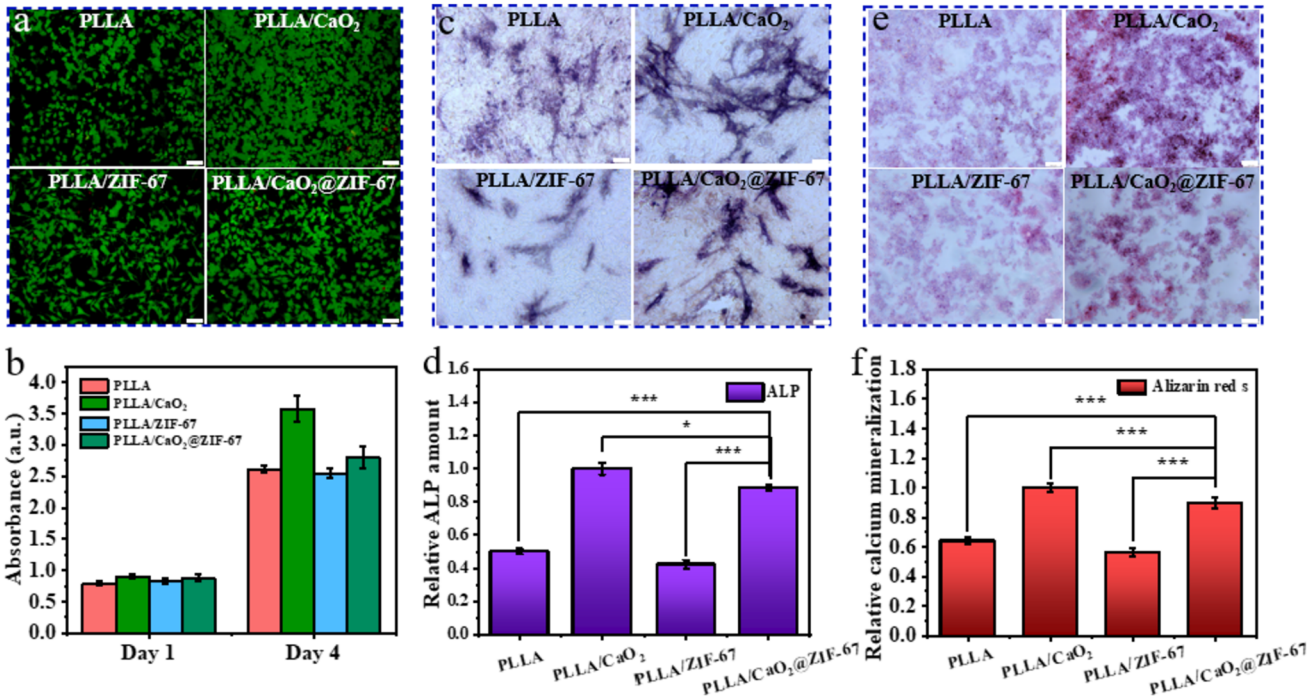

Figure 6 Cytocompatibility and osteogenic properties of scaffolds. **a** Live/dead fluorescent staining images of mBMSCs cultured with PLLA, PLLA/CaO_2, PLLA/ZIF-67 and PLLA/CaO_2@ZIF-67 scaffolds for 4 days. Scale bars are 100 μm. **b** CCK-8 results of mBMSCs cultured with different scaffolds for 1 and 4 days. **c** ALP staining images of the cells cultured with different scaffolds for 7 days. Scale bars are 50 μm. **d** Statistical analysis of ALP staining using ImageJ software. **e** Alizarin Red S staining images of the cells cultured with different scaffolds for 14 days. Scale bars are 100 μm. **f** Corresponding statistical analysis of Alizarin Red S staining using ImageJ software. p values were calculated by Student's t-test ($^{*}p < 0.05$; $^{**}p < 0.01$; $^{***}p < 0.001$).

promoted the osteogenic differentiation of stem cells, while cobalt ions inhibited cell proliferation and differentiation [47, 49]. Figure 6f shows the corresponding semi-quantitative analysis, which is consistent with the previous analysis.

Conclusions

In conclusion, the pH-responsive CaO_2@ZIF-67 core–shell particles were successfully synthesized by an *in-situ* growth method, and the PLLA/CaO_2@ZIF-67 scaffolds were subsequently prepared by selective laser sintering technology. In the weakly acidic microenvironment of the tumor, CaO_2@ZIF-67 particles are decomposed rapidly, and releasing cobalt ions and generating hydrogen peroxide, thus significantly improves the efficacy of chemodynamic antitumor effect on account of Fenton-like reaction to produce a large number of hydroxyl radicals, and its killing ratio of MG-63 cells reached to 84.64%. Meanwhile, the PLLA/CaO_2@ZIF-67 scaffolds also promote the proliferation and osteogenic differentiation of mBMSCs. Therefore, the prepared scaffolds with excellent antitumor effect and osteogenic ability have great potential in the treatment of bone tumors.

Acknowledgements

This study was supported by the following funds: (1) The Natural Science Foundation of China (51935014, 52165043, 52105352, 82072084, 81871498); (2) JiangXi Provincial Natural Science Foundation of China (2020ACB214004, 20202BAB214011); (3) The Provincial Key R & D Projects of Jiangxi (20201BBE51012); (4) The Project of State Key Laboratory of High Performance Complex Manufacturing; (5) High-level Talents Scientific Research Initiation Project of Jiangxi University of Science and Technology (205200 100487); and (6) Science and Technology Research Project of Education Department of Jiangxi Province (GJJ200863); (7) The Natural Science Foundation of China (81960880); (8) Guangdong Province Higher

Vocational Colleges & Schools Pearl River Scholar Funded Scheme (2018); (9) Technology Innovation Platform Project of Shenzhen Institute of Information Technology 2020 (PT2020E002).

Declarations

Conflict of interest The authors declare that they have no known competing financial interests or personal relationships that could have appeared to influence the work reported in this paper.

References

[1] Jia CY, Guo YX, Wu FG (2022) Chemodynamic therapy via fenton and fenton-like nanomaterials: strategies and recent advances. Small 18(6):2103868. https://doi.org/10.1002/smll.202103868

[2] Wang XW, Zhong XY, Liu Z, Cheng L (2022) Recent progress of chemodynamic therapy-induced combination cancer therapy. Nano Today 35:100946. https://doi.org/10.1016/j.nantod.2020.100946

[3] Meng XY, Zhang XZ, Liu M, Cai B, He NY, Wang ZF (2020) Fenton reaction-based nanomedicine in cancer chemodynamic and synergistic therapy. Appl Mater Today 21:100864. https://doi.org/10.1016/j.apmt.2020.100864

[4] Cao W, Jin MY, Yang K, Chen B, Xiong MM, Li X, Cao GD (2021) Fenton/Fenton-like metal-based nanomaterials combine with oxidase for synergistic tumor therapy. J Nanobiotechnol 19(1):1–35. https://doi.org/10.1016/j.apmt.2020.100864

[5] Li SL, Jiang P, Jiang FL, Liu Y (2021) Recent advances in nanomaterial-based nanoplatforms for chemodynamic cancer therapy. Adv Funct Mater 31(22):2100243. https://doi.org/10.1002/adfm.202100243

[6] Yang ML, Shuai Y, Yang YW, Zeng D, Peng SP, Tian ZJ, Shuai CJ (2022) In situ grown rare earth lanthanum on carbon nanofibre for interfacial reinforcement in Zn implants. VIRTUAL PHYS PROTOTY 17(3):700–717. https://doi.org/10.1080/17452759.2022.2053929

[7] Shuai C, Yuan X, Shuai Y, Qian G, Yao J, Xu W, Peng S,Yang W (2022) Nitrogen-doped carbon-ZnO heterojunction derived from ZIF-8: a photocatalytic antibacterial strategy for scaffold. Mater Today Nano 18:100210. https://doi.org/10.1016/j.mtnano.2022.100210

[8] Yang YW, Zan J, Shuai Y et al (2022) in situ growth of a metal-organic framework on graphene oxide for the chemo-photothermal therapy of bacterial infection in bone repair. ACS Appl Mater Inter. https://doi.org/10.1021/acsami.2c04841

[9] Tang ZM, Liu YY, He MY, Bu WB (2019) Chemodynamic therapy: tumour microenvironment-mediated Fenton and Fenton-like reactions. Angew Chem Int Edit 58(4):946–956. https://doi.org/10.1002/anie.201805664

[10] Lin LS, Song JB, Song L et al (2018) Simultaneous Fenton-like ion delivery and glutathione depletion by MnO2-based nanoagent to enhance chemodynamic therapy. Angew Chem Int Edit 130(18):4996–5000. https://doi.org/10.1002/anie.201712027

[11] Zhang C, Bu W, Ni D et al (2016) Synthesis of iron nanometallic glasses and their application in cancer therapy by a localized Fenton reaction. Angew Chem Int Edit 128(6):2141–2146. https://doi.org/10.1002/anie.201510031

[12] Huo MF, Wang LY, Chen Y, Shi JL (2017) Tumor-selective catalytic nanomedicine by nanocatalyst delivery. Nat Commun 8(1):1–12. https://doi.org/10.1038/s41467-017-00424-8

[13] Gao ST, Jin Y, Ge K et al (2019) Self-supply of O_2 and H_2O_2 by a Nanocatalytic medicine to enhance combined chemo/Chemodynamic therapy. Adv Sci 6(24):1902137. https://doi.org/10.1002/advs.201902137

[14] Tang ZM, Liu YY, Ni DL et al (2020) Biodegradable nanoprodrugs:"delivering" ROS to cancer cells for molecular dynamic therapy. Adv Mater 32(4):1904011. https://doi.org/10.1002/adma.201904011

[15] Liu B, Bian YL, Liang S et al (2021) One-step integration of tumor microenvironment-responsive calcium and copper peroxides nanocomposite for enhanced chemodynamic/ion-interference therapy. ACS Nano 16(1):617–630. https://doi.org/10.1021/acsnano.1c07893

[16] Trachootham D, Alexandre J, Huang P (2009) Targeting cancer cells by ROS-mediated mechanisms: a radical therapeutic approach? Nat Rev Drug Discov 8(7):579–591. https://doi.org/10.1038/nrd2803

[17] He CC, Zhang XJ, Xiang GY (2020) Nanoparticle facilitated delivery of peroxides for effective cancer treatments. Biomater Sci UK 8(20):5574–5582. https://doi.org/10.1039/d0bm01265c

[18] Dong SM, Dong YS, Liu B et al (2022) Guiding transition metal-doped hollow cerium tandem nanozymes with elaborately regulated multi-enzymatic activities for intensive chemodynamic therapy. Adv Mater 34(7):2107054. https://doi.org/10.1002/adma.202107054

[19] He CC, Zhang XJ, Chen C et al (2021) A solid lipid coated calcium peroxide nanocarrier enables combined cancer chemo/chemodynamic therapy with O2/H2O2 self-sufficiency. Acta Biomater 122:354–364. https://doi.org/10.1016/j.actbio.2020.12.036

[20] Liu CH, Cao Y, Cheng YR, Wang DD, Xu TL, Su L, Zhang XJ, Dong HF (2020) An open source and reduce expenditure ROS generation strategy for chemodynamic/photodynamic

synergistic therapy. Nat Commun 11(1):1–9. https://doi.org/10.1038/s41467-020-15591-4

[21] Chu SL, Shi XL, Tian Y, Gao FX (2022) pH-Responsive polymer nanomaterials for tumor therapy. Front Oncol 12. https://doi.org/10.3389/fonc.2022.855019

[22] Deng F, Wu P, Qian GW, Shuai Y, Zhang LM, Peng SP, Shuai CJ, Wang GY (2022) Silver-decorated black phosphorus: a synergistic antibacterial strategy. Nanotechnology 33(24):245708. https://doi.org/10.1088/1361-6528/ac5aee

[23] Qi FW, Gao XW, Shuai Y, Peng SP, Deng YW, Yang S, Yang YW, Shuai CJ (2022). Magnetic-driven wireless electrical stimulation in a scaffold. Compos Part B Eng 237:109864. https://doi.org/10.1016/j.compositesb.2022.109864

[24] Qian JF, Sun FA, Qin LZ (2012) Hydrothermal synthesis of zeolitic imidazolate framework-67 (ZIF-67) nanocrystals. MATER LETT 82:220–223. https://doi.org/10.1016/j.matlet.2012.05.077

[25] Zhong GH, Liu DX, Zhang JY (2018) The application of ZIF-67 and its derivatives: adsorption, separation, electrochemistry and catalysts. J Mater Chem A 6(5):1887–1899. https://doi.org/10.1039/c7ta08268a

[26] Feng XH, Carreon MA (2015) Kinetics of transformation on ZIF-67 crystals. J Cryst Growth 418:158–162. https://doi.org/10.1016/j.jcrysgro.2015.02.064

[27] Lashgari SM, Yari H, Mahdavian M, Ramezanzadeh, B, Bahlakeh, G, Ramezanzadeh, M (2021) Application of nanoporous cobalt-based ZIF-67 metal-organic framework (MOF) for construction of an epoxy-composite coating with superior anti-corrosion properties. Corros Sci 178:109099. https://doi.org/10.1016/j.corsci.2020.109099

[28] Guo XL, Xing TT, Lou YB, Chen JX (2016) Controlling ZIF-67 crystals formation through various cobalt sources in aqueous solution. J Solid State Chem 235:107–112. https://doi.org/10.1016/j.jssc.2015.12.021

[29] Jiang Y, Lu Y, Lei LL, et al (2021) Near-infrared light-triggered synergistic antitumor therapy based on hollow ZIF-67-derived Co3S4-indocyanine green nanocomplex as a superior reactive oxygen species generator. Mat Sci Eng C Mater 130:112465. https://doi.org/10.1016/j.msec.2021.112465

[30] Ma YS, Xu HH, Sun B, Du SL, Cui S, Zhang L, Ding N, Yang DZ (2021) pH-responsive oxygen and hydrogen peroxide self-supplying nanosystem for photodynamic and chemodynamic therapy of wound infection. Acs Appl Mater Inter 13(50):59720–59730. https://doi.org/10.1021/acsami.1c19681

[31] Shuai CJ, Yang F, Shuai Y, Peng SP, Chen SJ, Deng YW, Feng P (2022) Silicon dioxide nanoparticles decorated on graphene oxide nanosheets and their application in poly (L-lactic acid) scaffold. J Adv Res. https://doi.org/10.1016/j.jare.2022.08.017

[32] Gao CD, Zeng ZH, Peng SP, Shuai CJ (2022) Magnetostrictive bulk Fe-Ga alloys prepared by selective laser melting for biodegradable implant applications. Mater Design 220:110861. https://doi.org/10.1016/j.matdes.2022.110861

[33] Shuai CJ, Wang ZC, Peng SP, Shuai Y, Chen YW, Zeng D, Feng P (2022) Water-responsive shape memory thermoplastic polyurethane scaffolds triggered at body temperature for bone defect repair. Mater Chem Front 6(11):1456–1469. https://doi.org/10.1039/d1qm01635k

[34] Shuai CJ, Chen X, He CX, Qian GW, Shuai Y, Peng SP, Deng YW, Yang WJ (2022) Construction of magnetic nanochains to achieve magnetic energy coupling in Scaffold. Biomater Res 26(1). https://doi.org/10.1186/s40824-022-00278-2

[35] Oladapo BI, Zahedi SA, Ismail SO, Omigbodun FT, Bowoto OK, Olawumi MA, Muhammad MA (2020) 3D printing of PEEK–cHAp scaffold for medical bone implant. Bio Des Manuf 4(1):44–59. https://doi.org/10.1007/s42242-020-00098-0

[36] Silva EPE, Huang BY, Helaehil JV et al (2021) In vivo study of conductive 3D printed PCL/MWCNTs scaffolds with electrical stimulation for bone tissue engineering. Bio Des Manuf 4(2):190–202. https://doi.org/10.1007/s42242-020-00116-1

[37] Feng P, Shen SP, Yang LYM, Kong Y, Yang S, Shuai CJ (2022) Vertical and uniform growth of MoS2 nanosheets on GO nanosheets for efficient mechanical reinforcement in polymer scaffold. Virtual Phys Prototy 18(1):e2115384. https://doi.org/10.1080/17452759.2022.2115384

[38] Qian YJ, Zhang J, Zhang YL, Chen JB, Zhou XF (2016) Degradation of 2, 4-dichlorophenol by nanoscale calcium peroxide: implication for groundwater remediation. Sep Purif Technol 166:222–229. https://doi.org/10.1016/j.seppur.2016.04.010

[39] Yan SL, Kim M, Salley SO, Ng KYS (2009) Oil transesterification over calcium oxides modified with lanthanum. Appl Catal A Gen 360(2):163–170. https://doi.org/10.1016/j.apcata.2009.03.015

[40] Zeglinski J, Piotrowski GP, Piękos R (2006) A study of interaction between hydrogen peroxide and silica gel by FTIR spectroscopy and quantum chemistry. J Mol Struct 794(1–3):83–91. https://doi.org/10.1016/j.molstruc.2006.01.043

[41] Wu JR, Zhang ZJ, Qiao CX, Yi CF, Xu ZS, Chen TY, Dai XF (2021) Synthesis of monodisperse ZIF-67@CuSe@PVP nanoparticles for pH-responsive drug release and

photothermal therapy. Acs Biomater Sci Eng 8(1):284–292. https://doi.org/10.1021/acsbiomaterials.1c01124

[42] Ni M, Ratner BD (2008) Differentiating calcium carbonate polymorphs by surface analysis techniques—an XPS and TOF-SIMS study. Surf Interface Anal 40(10):1356–1361. https://doi.org/10.1002/sia.2904

[43] Wang ZP, Zhang YG, Tan ZC, Li QH (2018) A wet process for oxidation-absorption of nitric oxide by persulfate/calcium peroxide. Chem Eng J 350:767–775. https://doi.org/10.1016/j.cej.2018.05.145

[44] Qin JN, Wang SB, Wang XC (2017) Visible-light reduction CO2 with dodecahedral zeolitic imidazolate framework ZIF-67 as an efficient co-catalyst. Appl Catal B Environ 209:476–482. https://doi.org/10.1016/j.apcatb.2017.03.018

[45] Niu YQ, Galluzzi M, Deng FM, et al (2022) A biomimetic hyaluronic acid-silk fibroin nanofiber scaffold promoting regeneration of transected urothelium. Bioeng Transl Med 7(2):e10268. https://doi.org/10.1002/btm2.10268

[46] Zhang YB, Liu XC, Zeng LD, Zhang J, Zuo JL, Zou J, Ding JX, Chen XS (2019) Polymer fiber scaffolds for bone and cartilage tissue engineering. Adv Funct Mater 29(36):1903279. https://doi.org/10.1002/adfm.201903279

[47] Li YC, Lin ZY, Wang XY, et al (2021) High-hydrophobic ZIF-8@ PLA composite aerogel and application for oil-water separation. Sep Purif Technol 270:118794. https://doi.org/10.1016/j.seppur.2021.118794

[48] Torii S, Kurihara A, Li XY, Yasumoto KI, Sogawa K (2011) Inhibitory effect of extracellular histidine on cobalt-induced HIF-1α expression. J Biochem 149(2):171–176. https://doi.org/10.1093/jb/mvq129

[49] Qian GW, Wen TC, Shuai Y, Wu XT, Zeng ZK, Peng SP, Shuai CJ (2022) Photothermal and photodynamic effects of g-C3N4 nanosheet/Bi2S3 nanorod composites with antibacterial activity for tracheal injury repair. Acs Appl Nano Mater. https://doi.org/10.1021/acsanm.2c03569

[50] Qi FW, Wang ZH, Shuai Y, Peng SP, Shuai CJ (2022) Sr2+ sustained release system augments bioactivity of polymer scaffold. Acs Appl Polym Mater 4(4):2691–2702. https://doi.org/10.1021/acsapm.2c00024

[51] Nakamura S, Matsumoto T, Sasaki JI, Egusa H, LEE KY, Nakano T, Sohmura T, Nakahira A, (2010) Effect of calcium ion concentrations on osteogenic differentiation and hematopoietic stem cell niche-related protein expression in osteoblasts. Tissue Eng Pt A 16(8):2467–2473. https://doi.org/10.1089/ten.tea.2009.0337

[52] Seol YJ, Park JY, Jung JW, Jang J, Girdhari R, Kim SW, Cho DW (2014) Improvement of bone regeneration capability of ceramic scaffolds by accelerated release of their calcium ions. Tissue Eng Pt A 20(21–22):2840–2849. https://doi.org/10.1089/ten.tea.2012.0726

[53] Fazeli N, Arefian E, Irani S, Ardeshirylajimi A, Seyedjafari E (2021) 3D-printed PCL scaffolds coated with nanobioceramics enhance osteogenic differentiation of stem cells. ACS Omega 6(51):35284–35296. https://doi.org/10.1021/acsomega.1c04015